Advanced Materials

ADVANCED MATERIALS
www.advmat.de

RESEARCH ARTICLE

Mild Coordination Enabled by Steric Hindrance Facilitates Fabrication of Large-Area Perovskite Solar Modules

Jialiang Liu[1] | Mengjie Li[2] | Jun Ji[3] | Zhiguo Zhao[2] | Meicheng Li[1]

[1]State Key Laboratory of Alternate Electrical Power System With Renewable Energy Sources, School of New Energy, North China Electric Power University, Beijing, China | [2]China Huaneng Clean Energy Research Institute, Beijing, China | [3]Beijing Huairou Laboratory, Beijing, China

Correspondence: Zhiguo Zhao (zg_zhao@qny.chng.com.cn) | Meicheng Li (mcli@ncepu.edu.cn)

Received: 26 October 2025 | **Revised:** 24 January 2026 | **Accepted:** 3 February 2026

Keywords: buried interfaces | diethyl sulfoxide | mild coordination | perovskite solar modules | steric hindrance

ABSTRACT

The scalable fabrication of high-efficiency perovskite solar modules is critically challenged by the difficulty in controlling crystallization homogeneity and mitigating buried interfacial defects across large-area substrates. The commonly used dimethyl sulfoxide (DMSO) can induce heterogeneous nucleation and is prone to remain trapped within the films. Herein, diethyl sulfoxide (DESO) is introduced, a volatile Lewis acid-base additive that leverages steric hindrance effects from its branched-chain structure to achieve mild coordination with PbI_2. This structural feature reduces the binding energy between DESO and PbI_2, which avoid the formation of complex metastable intermediate phases. Moreover, the low binding energy of DESO enables its complete removal during vacuum quenching via rapid evaporation, effectively suppressing void formation at the buried interfaces during the subsequent annealing. The resultant perovskite films yield perovskite solar modules (PSMs) with power conversion efficiencies (PCEs) of 22.9% (11.2 cm^2, aperture area) and 20.8% (692 cm^2, aperture area) via scalable processes. These devices exhibit operational stability, retaining >96% of their initial PCE after 2000 h under continuous 1-sun illumination and >95% PCE following 2000 h damp-heat testing (85°C/85% RH).

1 | Introduction

Perovskite single-junction solar cells have achieved remarkable power conversion efficiencies (PCEs) of 27.0% at laboratory scales [1]. However, significant efficiency losses occur during upscaling, where certified champion PCEs drop to 21.1% (843.5 cm^2 designated illumination area) for sub-modules and 18.1% (7218 cm^2 total area) for standard modules [2]. Further scaling to 2.82 m^2 modules reduces PCE to 17.04% [3], creating a critical efficiency gap that impedes commercialization. Minimizing the cell-to-module efficiency loss requires the production of high-crystallinity, uniform perovskite films across large-area substrates. Current strategies focus on solvents, additives and composition to control crystallization kinetics and structural evolution. Solvents prove especially crucial for scalable and large-area perovskite film fabrication due to their physicochemical properties, such as vapor pressure, viscosity and coordination ability [4–8]. Solution processing involves coating the substrate with a precursor solution, followed by solvent removal through evaporation or drying to form a perovskite or an intermediate phase. A subsequent thermal annealing step is then applied to convert this into the crystalline perovskite phase [9]. For large-scale fabrication of perovskite solar modules (PSMs), the increased substrate size prolongs the slot-die coating process [10]. This necessitates solvents with sufficient coordination strength to stabilize the wet film over the larger area. However, effective solvent removal techniques, such as vacuum quenching or air knife-assisted, require that the solvent system be highly volatile [11]. Thus, an ideal solvent should mildly coordinate with PbI_2 to meet the time window required for large-area slot-die

coating, while remaining volatile enough for rapid removal during vacuum quenching.

The commonly used Lewis basic solvent dimethyl sulfoxide (DMSO) stabilizes photovoltaic α-$FAPbI_3$ through coordination with Lewis acidic sites (specifically Pb^{2+} ions) [12–16]. However, DMSO is prone to remaining trapped within the films, leading to defective interfaces [17]. Moreover, the strong coordination between DMSO and PbI_2 leads to multiple nucleation pathways from metastable intermediate phases during annealing [18]. These issues present critical challenges for obtaining homogeneous and highly crystalline perovskite films. In contrast to anti-solvent methods, industrial techniques like the N_2-knife and vacuum quenching rely on pressure-gradient-driven mechanisms, which result in slower solvent evaporation kinetics [19–21]. This inherent limitation leads to the entrapment and accumulation of DMSO at the buried interface [22], which induces void formation during annealing as the solvent escapes. For example, Chen et al. observed that perovskite crystallization via one-step solution deposition initiates at the film-air interface, rapidly forming a solid shell that entraps the DMSO-rich wet film, with approximately 10% of the solvent remaining confined in the bottom layer. This trapped solvent subsequently escapes during annealing, coupling with volumetric shrinkage to generate voids near the perovskite-substrate interface [23–25]. Furthermore, Li et al. and Pu et al. demonstrated that residual solvent trapped in precursor films governs intermediate phase evolution during crystallization, enabling multiple nucleation pathways from various intermediate phases. These pathways induce compositional heterogeneity and lattice strain, ultimately driving anisotropic grain growth with discontinuous morphology [18, 26]. Additionally, Liu et al. found that DMSO induced instability of intermediates, provoked an unfavorable δ-to-α phase transition, and left behind a residual δ-phase in the annealed $FAPbI_3$ film [27]. These issues collectively contribute to interface defects as well as anisotropic grain growth through multiple nucleation pathways.

Herein, we report that the Lewis basic solvent diethyl sulfoxide (DESO) utilizes steric hindrance [13, 28] from its branched-chain structure to achieve mild coordination with PbI_2. This mild coordination provides a sufficient time window for large-area slot-die coating. Moreover, the rapid evaporation of DESO during vacuum quenching prevents void formation at the buried interface while simultaneously avoiding the transition through multiple intermediate phases, thereby yielding high-quality perovskite films. PSMs fabricated via scalable processes achieved PCEs of 22.9% (11.2 cm^2) and 20.8% (692 cm^2), with exceptional operational stability retaining >96% of their initial PCE after 2000 h under continuous 1-sun illumination and >95% PCE following 2000 h damp-heat testing (85°C/85% RH).

2 | Results and Discussion

2.1 | Steric-Confined Coordination

The physicochemical properties of the solvent usually influence the processing window, volatility and structural evolution, thereby directly influencing large-area film homogeneity and crystallinity [29, 30]. With respect to key solvent parameters including boiling point, vapor pressure and donor number, DESO exhibits a higher boiling point, lower vapor pressure [31] and higher donor number [32] compared to DMSO as shown in Figure 1b. Based on these properties alone, DESO would evaporate more slowly. However, during perovskite film fabrication and thermogravimetric analysis (TGA), we observed that DESO evaporates more rapidly than DMSO. As shown in Figure 1c, the DESO-based system undergoes a sharp mass loss in the temperature range of 140–160 °C, whereas the DMSO-based system remains stable until approximately 200 °C. Furthermore, we calculated the binding energies between each solvent and PbI_2. Figure 1a illustrates the molecular structures and electrostatic potential (ESP) [33] distributions of DMSO and DESO. Similar to DMSO, the region of low ESP (indicating high electron density) in DESO is localized around the sulfur, which facilitates coordination with PbI_2. We used density functional theory (DFT) [34] to calculate the interaction energy between PbI_2 and the two coordination molecules (Figure S1). The interaction energy between PbI_2 and DESO (−0.58 eV) is lower than that between PbI_2 and DMSO (−0.91 eV). This might be due to the steric hindrance effect caused by its branched structure [28, 35]. We further investigated the molecular interactions between DESO and perovskite precursors through Fourier-transform infrared (FTIR), as shown in Figure 1d. The S = O stretching vibration of DESO exhibited a notable redshift from 1017 to 1004 cm^{-1}, while that of DMSO shifted from 1027 to 1022 cm^{-1} upon coordination with PbI_2, indicating the formation of coordination bond by sharing the lone pair electrons in oxygen with Pb^{2+}. After the introduction of formamidinium iodide (FAI), DMSO showed further redshift from 1022 to 1019 cm^{-1}. In contrast, DESO displayed blueshift from 1004 to 1008 cm^{-1}, which likely arises from competitive coordination between I^- and the solvent for Pb^{2+} [36, 37]. FAI introduces excess iodide, shifting the equilibrium toward higher order iodoplumbate species (PbI_3^-/PbI_4^{2-}). This partially displace DESO from Pb^{2+} and is more readily released during film formation, which would facilitate conversion to the black-phase $FAPbI_3$. Further, we performed Raman spectroscopy and observed the same trend as shown in Figure 1e. Upon addition of PbI_2, the S = O stretching vibration in both solvents exhibits a clear redshift, confirming coordination between the sulfoxide oxygen and Pb^{2+}. When FAI is further introduced to form the perovskite precursor, the divergence in solvent behavior becomes even more pronounced. In the DMSO-based system, the S = O peak continues to redshift, demonstrating that DMSO maintains robust coordination with Pb^{2+} even in the presence of FAI. In contrast, in the DESO-based system, the S = O peak does not undergo further redshift; instead, it remains near 1019 cm^{-1}, indicating that DESO is partially displaced from Pb^{2+} by iodide ions derived from FAI. This result aligns well with the FTIR data shown in Figure 1d. Dynamic light scattering (DLS) further supports that more FA^+ and I^- ions participate in reactions with PbI_2, leading to a decrease in the size of perovskite colloidal clusters [38]. As shown in Figure 1f, the colloidal clusters in perovskite precursor solution with DESO are significantly smaller than those with DMSO. Figure 1g shows the schematic diagram of the possible phase evolution of the nucleation and crystallization of FA-based mixed anion perovskites during the film-forming process. The strong binding energy between DMSO and PbI_2 results in not only its entrapment at the bottom interface but also the promotion of anisotropic grain growth via multiple nucleation pathways. In contrast, DESO leverages steric hindrance from its

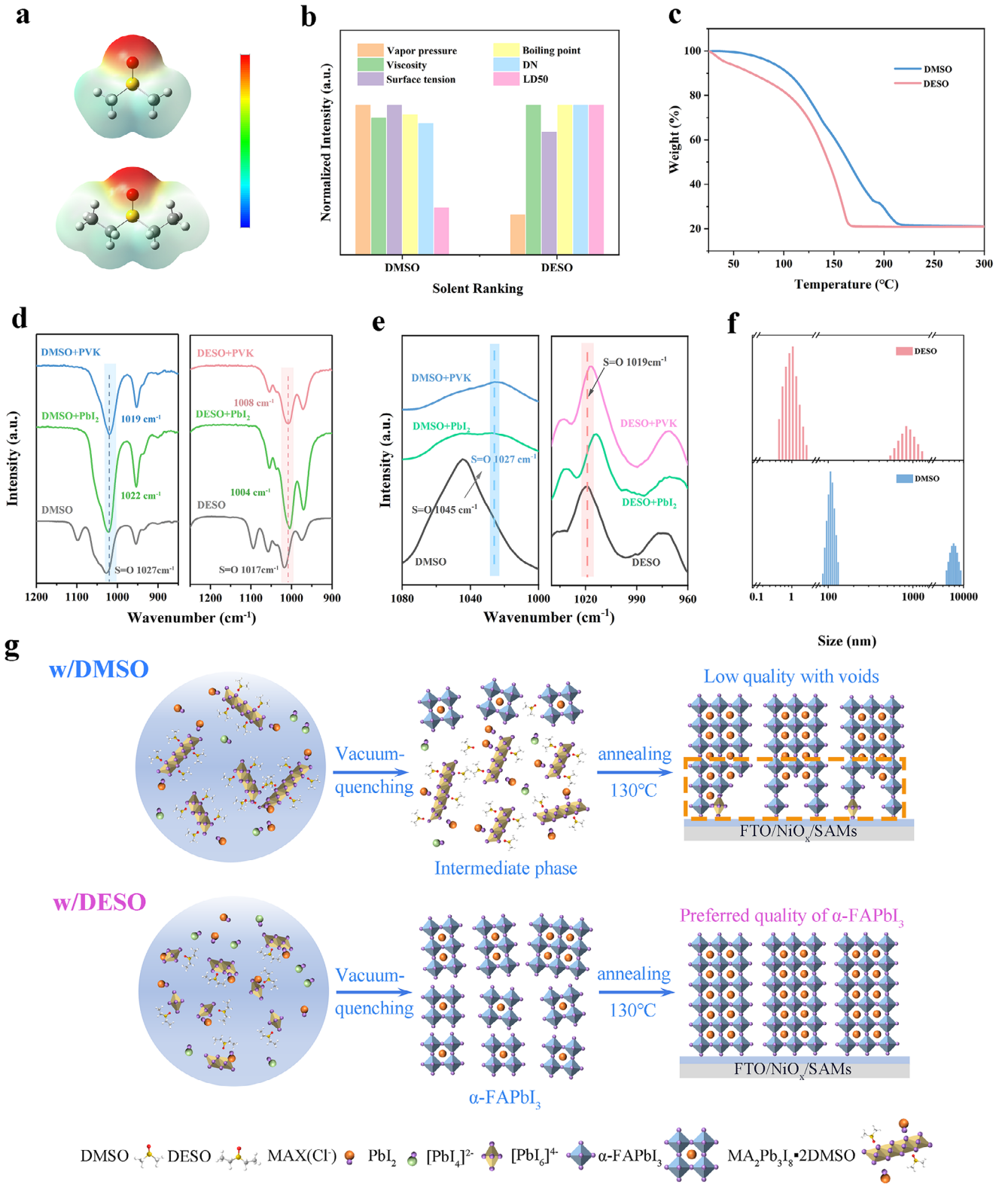

FIGURE 1 | (a) Molecular electrostatic potential maps of DMSO and DESO; (b) Comparison of key solvent properties between DMSO and DESO, where DN denotes the donor number and LD_{50} refers to the median lethal dose; (c) Thermogravimetric analysis (TGA) curves of perovskite precursor solutions with DMSO or DESO. (d) Fourier transform infrared (FTIR) spectra of PbI_2 and $FAPbI_3$ (PVK) in DMSO and DESO solvents; (e) Raman curves of perovskite precursor solutions with DMSO or DESO; (f) Dynamic light scattering (DLS) particle size distribution of perovskite precursor solution; (g) Schematic diagram of the possible phase evolution of the nucleation and crystallization of FA-based mixed anion perovskites during the film-forming process with DMSO or DESO.

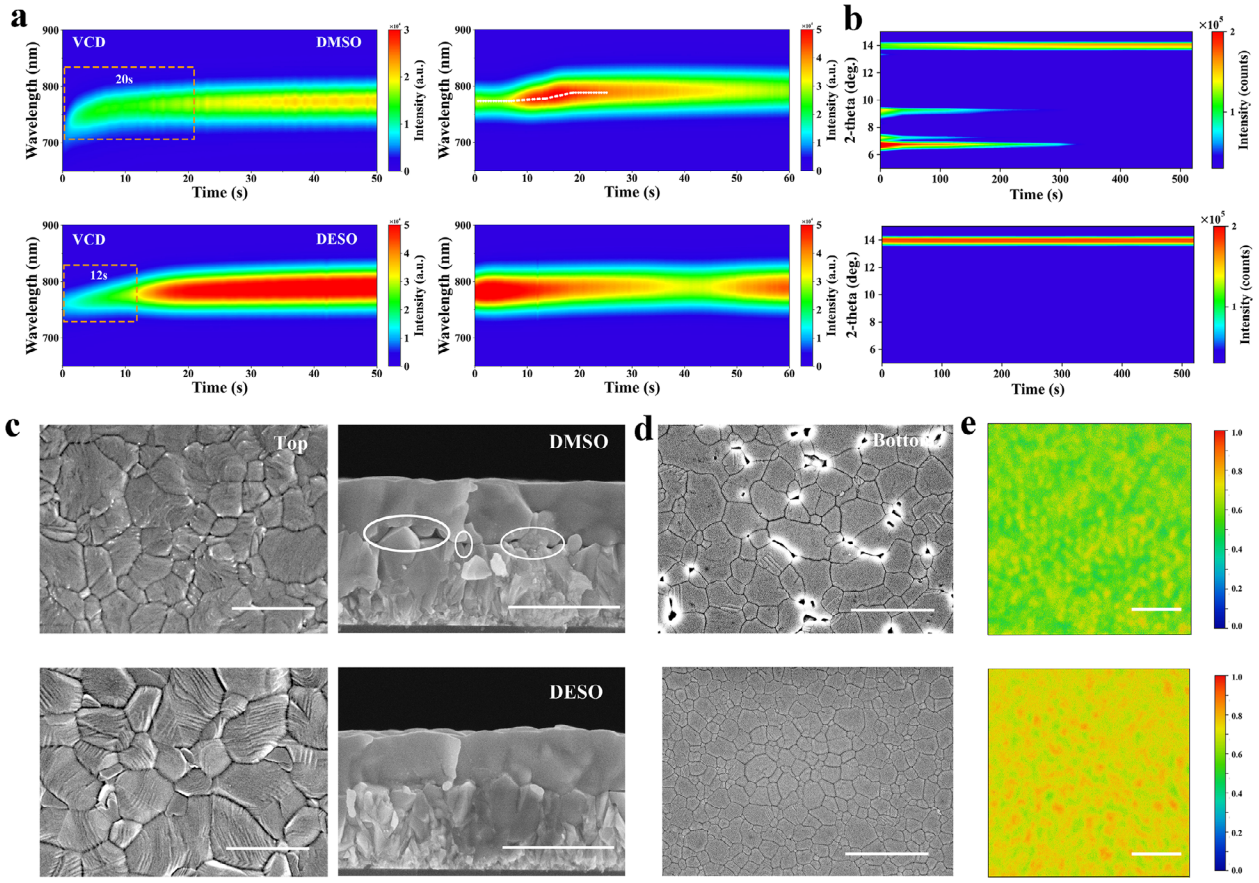

FIGURE 2 | Effect of DMSO and DESO treatment on perovskite precursors and crystallization process: (a) In situ photoluminescence (PL) spectra during vacuum quenching and annealing. Top: DMSO-treated; Bottom: DESO-treated; (b) In situ X-ray diffraction (XRD) patterns of perovskite films treated with DMSO and DESO at different annealing and times; (c) The surface and cross-section SEM images of perovskite films. Top: DMSO-treated; Bottom: DESO-treated. Scale bars, 1 μm; (d) SEM images of the perovskite-substrate interfaces of the blade-coated perovskite films that were peeled off from glass substrates; (e) PL mapping imaging of perovskite films. Top: DMSO-treated; Bottom: DESO-treated. Scale bars, 5 μm.

branched-chain structure to achieve mild coordination with PbI_2. This mild interaction suppresses void formation at the buried interfaces and improves the quality of perovskite films.

2.2 | Crystallization Dynamics and Morphology

The interaction between Lewis basic solvent and perovskite directly affects the thermodynamics and kinetics of α-$FAPbI_3$ formation, which often occurs rapidly during the vacuum quenching and initial annealing stages [19]. Therefore, in order to investigate the crystallization pathway and structural evolution during solvent evaporation and annealing under ambient conditions, we carried out in situ photoluminescence (PL), in situ UV–vis and in situ XRD [39]. As illustrated in Figure 2a, DMSO-treated perovskite films exhibited delayed crystallization kinetics, with a weak perovskite signal emerging after 20 s of vacuum quenching. In contrast, DESO-treated films showed the perovskite peak within 12 s, and its peak intensity was higher than that of the DMSO-treated sample. This accelerated crystallization may be attributed to the rapid evaporation of DESO. Moreover, the maximum PL peak position of the DMSO-based film showed a red shift from 772 to 785 nm during the first 20 s of annealing. This significant peak shift may be attributed to the transformation from intermediate phases to the perovskite phase. However, a minimal peak shift was observed in the DESO sample (Figure S2) during annealing, further supporting that the perovskite phase had formed in the DESO-treated films after vacuum quenching, which is consistent with the following in situ XRD results. In the supporting information (Video S1), a video showing the in situ PL evolution during the vacuum quenching process of perovskite films treated by DMSO or DESO is provided. We further performed in situ UV–vis spectroscopy to monitor crystallization dynamics during annealing [40]. As shown in Figure S3, the DESO-treated film shows distinct perovskite absorption features within the initial 10 s, indicating rapid perovskite nucleation driven by faster DESO evaporation. Conversely, DMSO-treated films showed no discernible absorption at the initial stage, which may be due to the formation of intermediate phases. In situ XRD characterization [41] further elucidated crystallization dynamics during annealing (Figure 2b; Figure S4). DMSO-treated films exhibited pronounced signatures of various intermediate [42] phases (at $2\theta = 6.68°$ and $9.24°$) that required prolonged annealing (100°C, 5 min) for complete elimination. For the DESO-treated film, it can directly form the perovskite phase after vacuum quenching. This might be due to the weak coordination that inhibits the formation of competing intermediate phases, which supports the in situ PL and in situ UV–vis. As shown in Figure S5, microscopic analysis of perovskite films after slot-die coating at different waiting times revealed that the DESO-based film

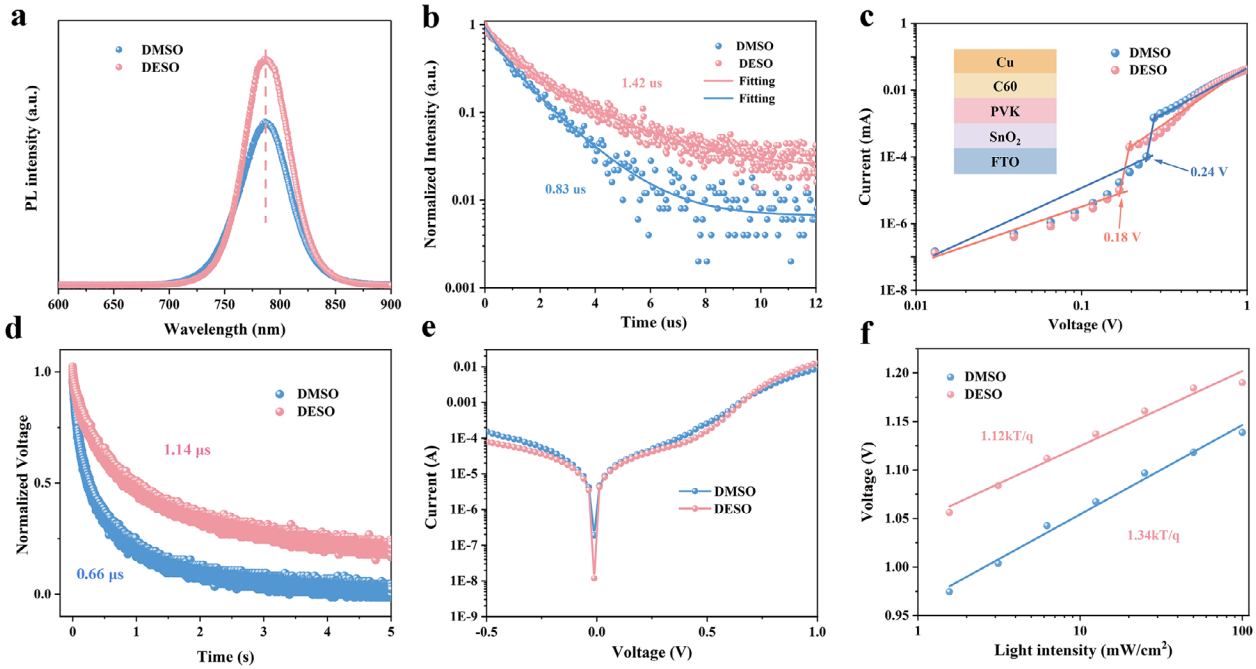

FIGURE 3 | Photoelectronic performance characterization of DMSO and DESO treated perovskite films and devices: (a) Steady–state photoluminescence (PL) spectra of perovskite films; (b) TRPL curves of the perovskite film; (c) Current density-voltage characteristics of devices with FTO/SnO_2/PVK/C60/Cu (electron-only); (d) Transient photovoltage (TPV) decay curves; (e) Dark current curves of PSCs; (f) V_{OC} Vs light intensity for PSMs.

began its morphological evolution after a 4 min delay, whereas the DMSO-based film exhibited a longer processing window due to its stronger coordination. Although DESO offers a shorter processing window than DMSO, it remains sufficient for large-area fabrication. At a typical coating speed of 10–12 mm s^{-1}, covering a 1.2-meter substrate takes only 100–120 s, which is well within the window of 240 s (4 min). Therefore, DESO satisfies the time window required for large-area slot-die coating and can be efficiently removed during vacuum quenching.

The crystallization quality and morphology of mixed-halide perovskites depend on the solvent evaporation rate and multiple nucleation pathways from various intermediate phases. We used scanning electron microscopy (SEM) to investigate the morphology of perovskite film treated by DMSO or DESO. As shown in Figure 2c, Figures S6 and S7, the DESO-treated film exhibits a slightly larger apparent grain size and a lower root-mean-square roughness (Rq) than the DMSO-treated perovskite film. Although the difference in apparent grain size [43, 44] is modest, cross-sectional SEM imaging of the DMSO-treated film reveals a significant number of pinholes at the buried interface. To more clearly examine the morphology of the buried interface, we delaminated the perovskite layer from the glass substrate using a UV-curable adhesive (Figure S8), thereby exposing the pristine underlying interface for direct characterization. As shown in Figure 2d, the DMSO-treated film reveals the presence of interfacial voids, whereas the DESO-treated sample displayed a dense film. This improvement may be due to the faster evaporation of DESO. In contrast, DMSO tend to remain trapped at the buried interface due to its strong interaction with PbI_2. As the solvent eventually escapes, it causes the formation of voids due to volume contraction [23]. To further evaluate the quality of the perovskite film, we performed PL mapping (Figure 2e) of perovskite films using a 520-nm laser [7]. Compared to the DMSO-treated film, the DESO-treated film exhibited stronger PL emission. This enhancement support that the mild coordination between DESO and PbI_2 can effectively accelerate solvent evaporation and suppress pinhole formation at the buried interface.

2.3 | Carrier Dynamics and Photovoltaic Performance

As shown in Figure 3a,b, steady–state PL and time-resolved photoluminescence (TRPL) were used to evaluate the non-radiative carrier recombination behavior of the perovskite films. DESO-treated film displayed stronger PL intensity, which is consistent with the PL Mapping results (Figure 2e). Moreover, the perovskite film fabricated by DESO showed longer carrier lifetimes (1.42 μs) than DMSO-treated films (0.83 μs). This enhancement directly correlates with suppressed non-radiative recombination due to the improved crystalline quality as evidenced by enlarged grains and reduced pinholes in SEM. The trap-state density was characterized by space-charge limited current (SCLC) on electron-only devices with a structure of FTO/SnO_2/PVK/C60/Cu. As depicted in Figure 3c, the trap-filled limit voltage threshold (V_{TFL}) of perovskite film treated with DESO and DMSO was 0.18 V and 0.24 V, respectively. This showed a lower trap state density in the DESO-treated films (1.66×10^{15} cm^{-3}) compared to that of the DMSO (2.21×10^{15} cm^{-3}). These findings are in agreement with the SEM morphology and TRPL spectra, thereby supporting the crucial role of DESO in the crystallization. To investigate the recombination dynamics of photogenerated carriers, a brief transient photovoltaic signal triggered by a laser pulse (337 nm,

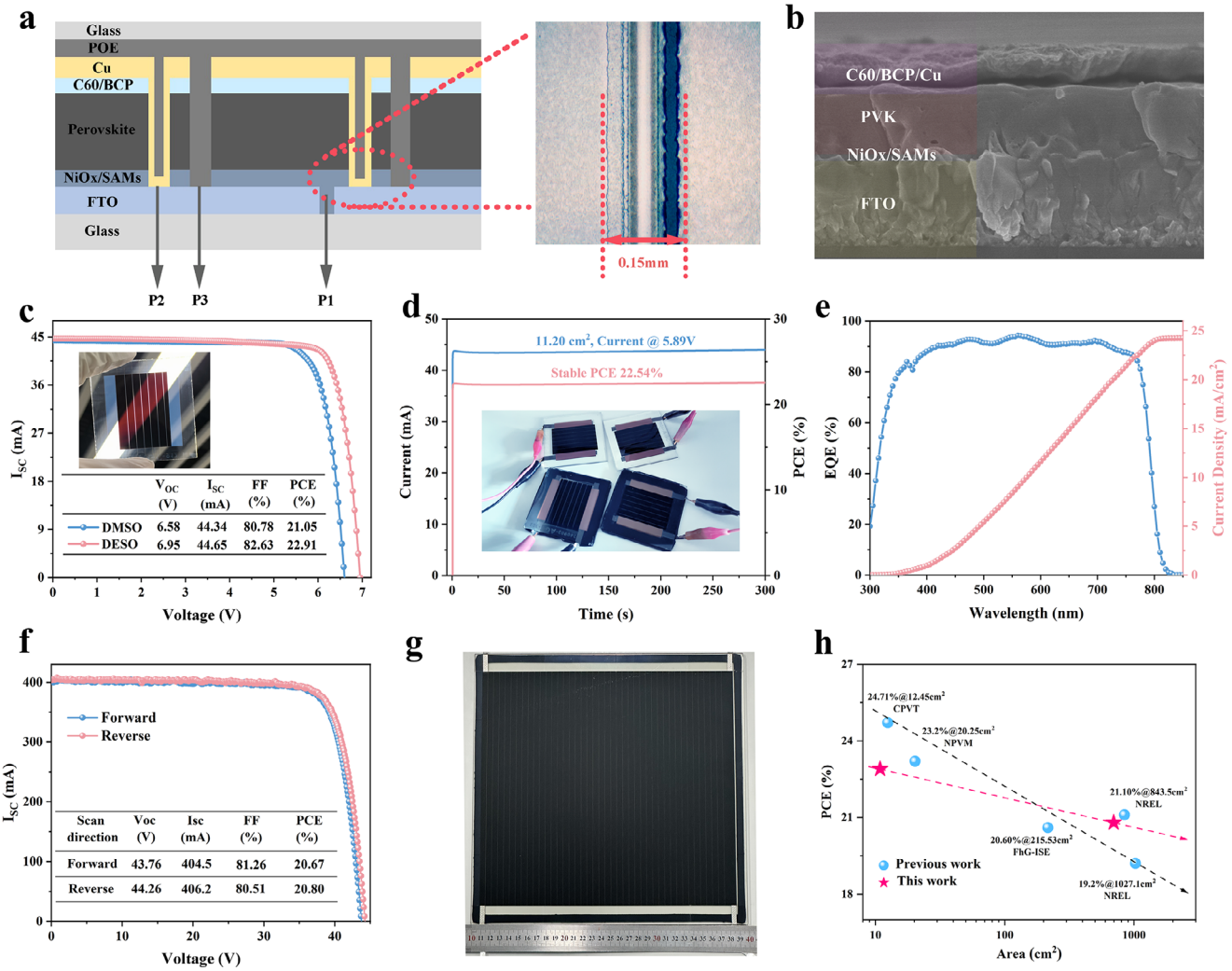

FIGURE 4 | Photoelectronic performance characterization of DMSO and DESO treated perovskite films and devices: (a) Schematic structure of the PSM and (b) Cross-sectional schematic of the perovskite module. (c) *I–V* curve of PSMs fabricated by DMSO or DESO on a 6.7 × 6.7 cm^2 substrate; (d) Steady–state power output curve at the maximum power point (MPP) for 300 s of the PSM by DESO-treated; (e) EQE spectra and integrated current density for the PSM fabricated by DESO; (f) *I–V* curve of the PSM fabricated by DESO on a 30 × 30 cm^2 substrate; (g) Photograph of the PSM fabricated by DESO on a 30 × 30 cm^2 substrate; (h) PCE diagrams for different module area: the red five-pointed star represents the efficiency obtained based on DESO and the blue sphere represents the efficiency reported by NERL. The slash represents the slope indicating a decrease in efficiency as the area increases.

4 ns) was used to determine the instantaneous photovoltaic (TPV) attenuation under AM 1.5G illumination. As shown in Figure 3d, the DESO-treated device exhibited a prolonged decay time constant of 1.14 μs compared to the 0.66 μs observed in the DMSO. In addition, we also conducted dark current density characterization under bias voltages ranging from −0.5 to 1 V (Figure 3e) to study the suppression of recombination processes in PSCs. The DESO treated perovskite device demonstrated superior dark current suppression with a current density of ~10^{-7}A cm^2, which is one order of magnitude lower than that of the DMSO treated device (~10^{-6}A cm^2). The reduced dark current density and prolonged carrier lifetime collectively demonstrate an improvement in the quality of the DESO-treated perovskite films, leading to enhanced charge extraction and transport properties. The dependence of open circuit voltage on light intensity (V_{OC} vs. light intensity) was tested to further analyze the charge recombination process in PSMs. As presented in Figure 3f, the DESO treated device exhibited an ideality factor of 1.12 kT/q, markedly lower than the 1.34 kT/q obtained from the DMSO. These results indicate that that the perovskite films regulated by DESO exhibit excellent carrier transport properties.

Building on the above studies of crystallization dynamics and structural evolution, we fabricated PSMs on 6.7 × 6.7 and 30 × 30 cm^2 FTO substrates to verify its scalability. The structural schematic diagram of PSMs and the dead zone (P1/P2/P3) of the laser scribing are shown in Figure 4a. Laser scribing dead zones (P1-P3) is 0.15 mm, and the geometric fill factor (GFF) is 97%. The SEM cross-sectional image of PSMs was shown in Figure 4b. The perovskite films exhibit almost no voids at the bottom interface in large dimensions. All reported photovoltaic parameters correspond to encapsulated modules based on the perovskite composition $Cs_{0.07}MA_{0.05}FA_{0.88}PbI_3$. The Current-voltage (*I–V*) characteristics of 6.7 × 6.7 cm^2 champion PSMs are presented in

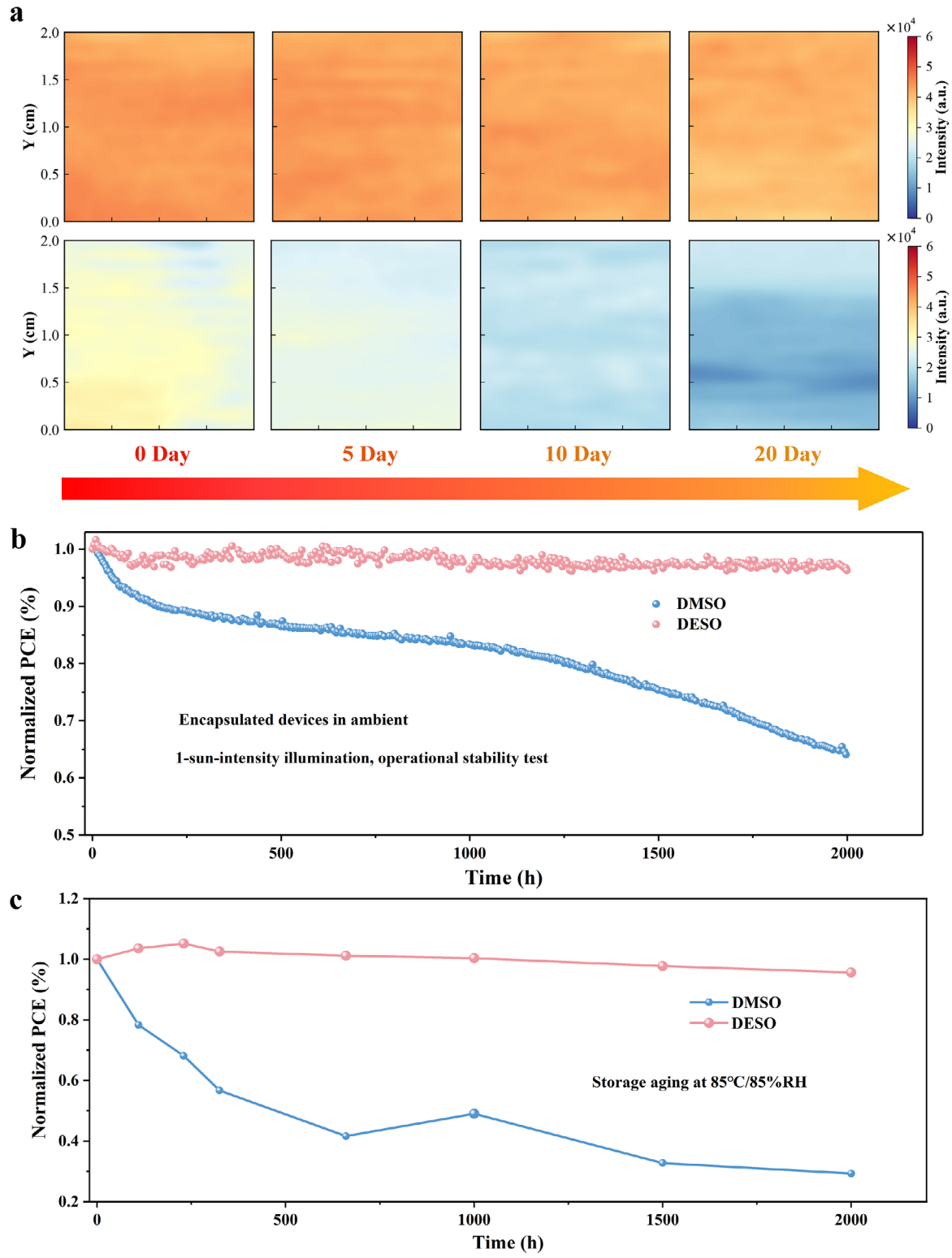

FIGURE 5 | Stability characterization of DMSO and DESO treated perovskite films and devices: (a) PL mapping of DMSO and DESO treated perovskite film after 20 days of aging; (b) MPPT curve of PSMs at 25°C; (c) Stability curve of PSMs under 85°C/85% relative humidity conditions.

Figure 4c. The module prepared by DESO exhibited a relatively high-power conversion efficiency of 22.9%, whereas the DMSO devices show lower efficiencies, primarily due to the decrease in open-circuit voltage (V_{OC}) and fill factor (FF), which implies an increase in defect densities [24]. The PSM fabricated by DESO exhibits an V_{OC} of approximately 1.16 V and an FF exceeding 82.63%, with a steady-state efficiency of 22.54% (Figure 4d). In contrast, PSMs treated by DMSO show a slight reduction in V_{OC} (1.10 V) and a moderate decrease in FF (80.78%) and a reduced PCE (21.05%). Figure S9 shows the forward and reverse *I-V* curves of PSMs by DESO on 6.7 × 6.7 cm^2 substrate. As referenced in the literature [45], the hysteresis index calculated based on

the *I-V* measurements is 0.44%, which may be attributed to the high-quality buried interface. Figure S10 shows the statistical distribution of PSMs photovoltaic parameters (V_{OC}, J_{SC}, FF and PCE). The average PCE, J_{SC}, V_{OC} and FF of PSMs processed by DESO is higher than that of DMSO, and the distribution is more concentrated, indicating better process reproductivity. The external quantum efficiency (EQE) spectra in Figure 4e show that the PSM fabricated by DESO exhibit strong photo response over a wide absorption rang. The integrated J_{SC} values derived from the EQE curves are 24.25 mA cm^2, which is consistent with the measured J_{SC} (24.67 mA/cm^2) in the *I–V* curves. To evaluate DESO's performance in larger-area devices, PSMs with an aperture area of 692.52 cm^2 were fabricated via slot-die coating on 30 × 30 cm^2 FTO substrates and the photograph of the real perovskite submodule is shown in Figure 4g. Figure S11 shows the electroluminescence (EL) images on the 30 × 30 cm^2 FTO substrates. The perovskite solar module fabricated by DESO exhibits brighter and more homogeneous EL than the DMSO-processed device. Figure 4f presents the *I–V* curves of the champion PSM fabricated by DESO. The PSM exhibits an V_{OC} of approximately 1.08 V, a current around 0.41 A, and an FF exceeding 80.11%, yielding a PCE of 20.8%. The PCE for forward scan is 20.67%. The hysteresis index calculated based on the *I–V* measurements from forward and reverse scans is 0.6%. In contrast, as shown in Figure S12, the PSM fabricated by DMSO showed a reduction in V_{OC} (1.02 V) and a decrease in FF (77.04%) and a reduced PCE (18.23%). Figure S13 shows the statistical comparison of photovoltaic parameters (V_{OC}, J_{SC}, FF, and PCE) for perovskite solar modules fabricated by DMSO or DESO on the 30 × 30 cm^2 substrate. The notable enhancement in V_{OC} and FF suggests reduced interfacial recombination and improved charge extraction, likely resulting from better film quality and reduced void formation at the buried interface. Figure 4h presents the PCE of PSMs for different module area. The red five-pointed star represents the efficiency obtained based on DESO and the blue sphere represents the efficiency reported by previous work. With the DESO solvent adjustment strategy, the fabricated modules exhibit a PCE close to the National Renewable Energy Laboratory (NERL) certified value of 21.1% at 843.5 cm^2. Moreover, as shown in Figure 4h, the efficiency shows only a minor decline as the device area is scaled from 11.2 cm^2 (22.91%) to 692.5 cm^2 (20.80%), demonstrating outstanding scalability. However, DMSO-treated PSMs show obvious decrease during upscaling from 11.2 cm^2 (21.05%) to 692.5 cm^2 (18.23%).

2.4 | Stability of Perovskite Film and Modules

PL mapping (Figure 5a) was used to investigate the degradation of encapsulated perovskite films under atmospheric conditions(25±3°C, 20±5% RH) [46]. The results showed that the DESO- treated film exhibited no significant decay in PL intensity over 20 days. In contrast, the DMSO-treated film showed obvious PL intensity decay. Statistical results of the PL peak intensity at different aging times were shown in Figure S14. The PL intensity of both DMSO- and DESO-treated perovskite films declines during aging, yet the DMSO film retains markedly higher and more slowly decaying emission, demonstrating superior stability over DESO. The UV–vis spectra of DMSO and DESO treated perovskite films were also analyzed. As shown in Figures S15 and S16, the DESO-treated film displayed no significant change in visible-range absorption after 20 days of aging. Conversely, significant degradation was observed for the DMSO-treated film. Furthermore, XRD was performed to investigate the change in crystal structure (Figure S17). Aged DMSO-processed films exhibited characteristic peaks corresponding to PbI_2, while DESO-treated film showed negligible signs of degradation. This observation aligned with the PL and UV–vis results, supporting the superior stability of the DESO-treated film.

The long-term operational stability of encapsulated PSMs was evaluated via maximum power point tracking (MPPT) under 1-sun equivalent illumination at room temperature. As shown in Figure 5b, the DESO treated PSM retained 96% of their initial PCE after 2000 h, demonstrating significantly improved illumination stability compared to that of the DMSO treated device. Continuous MPPT under 1-sun illumination at 85°C was performed to evaluate its high temperature stability (Figure S18). The DESO treated PSMs maintained 80% of its initial PCE after 1000 h of illumination at 85°C, showing marked improvement over the DMSO. Simultaneously, the stability of encapsulated PSMs under 85°C/85% RH conditions was examined. As shown in Figure 5c, the DESO treated device retained >95% of its initial efficiency after 2000 h of damp-heat testing. The better stability of DESO-treated PSMs might be attributed to the high-quality perovskite film.

3 | Conclusions

In summary, we demonstrate that DESO leverages steric hindrance from its branched-chain structure to achieve mild coordination with PbI_2. This structural feature reduces the binding energy between DESO and PbI_2, effectively enabling rapid solvent evaporation during vacuum quenching and suppressing the formation of complex metastable intermediate phases. Consequently, DESO promotes a single crystallization pathway and effectively prevents void formation at buried interfaces, yielding homogeneous, highly crystalline perovskite films. In contrast, the commonly used DMSO tends to induce heterogeneous nucleation and residual solvent entrapment, leading to interfacial voids and defective films. Scalable processes fabricated PSMs with efficiencies of 22.9% (11.2 cm^2) and 20.8% (692 cm^2), demonstrating excellent scalability and minimal efficiency loss upon upscaling. These devices also exhibited exceptional operational stability, retaining >96% of their initial PCE after 2000 h under continuous 1-sun illumination and >95% PCE following 2000 h of damp-heat testing (85°C/85% RH). This work underscores the critical role of solvent molecular design in regulating crystallization dynamics and interfacial quality, providing a practical strategy for the industrial-scale fabrication of high-performance and stable perovskite solar modules.

Acknowledgements

This work was supported partially by the Key Research and Development Program sponsored by the Ministry of Science and Technology (MOST) (Grant No. 2022YFB4200301), National Natural Science Foundation of China (Grant Nos. 52232008, 51972110, 52102245 and 52072121), Beijing Natural Science Foundation (No. 26JL001), Huaneng Group Headquarters Science and Technology Project (No. HNKJ20-H88), the Fundamental

Research Funds for the Central Universities (Nos. 2023MS042 and 2023MS047) and the NCEPU "Double First-Class" Program.

Conflicts of Interest

The authors declare no conflicts of interest.

Data Availability Statement

The data that support the findings of this study are available from the corresponding author upon reasonable request.

References

1. "National Renewable Energy Laboratory," Best Research-Cell Efficiency Chart, https://www.nrl.gov/pv/cell-efficiency.

2. M. A. Green, E. D. Dunlop, M. Yoshita, et al., "Solar Cell Efficiency Tables (Version 66)," *Progress in Photovoltaics: Research and Applications* 33 (2025): 795–810.

3. "The 2.82 m^2 perovskite module produced by Geegolight Energy's GW-scale production line has achieved a steady-state power output of 480.5 W, as rigorously tested by TÜV Rheinland, a globally recognized authoritative body," This corresponds to a full-area steady-state efficiency of 17.04%, setting an industry record for the highest efficiency of large-area perovskite modules, https://www.utmolight.com/20492/145551.html.

4. Y. Wang, C. Lu, M. Liu, et al., "Solvent-Assisted Reaction for Spontaneous Defect Passivation in Perovskite Solar Cells," *Nature Photonics* 19 (2025): 985–991.

5. Y. Zhang, X. Sun, Q. Wang, et al., "Solvent Environment Engineering for Reliable Fabrication of Perovskite Solar Cells in Air With a Wide Humidity Range," *Advanced Energy Materials* 15 (2025): 2500156.

6. X. Huang, G. Deng, S. Zhan, et al., "Solvent Gaming Chemistry to Control the Quality of Halide Perovskite Thin Films for Photovoltaics," *ACS Central Science* 8 (2022): 1008–1016.

7. S. Du, H. Huang, Z. Lan, et al., "Inhibiting Perovskite Decomposition by a Creeper-inspired Strategy Enables Efficient and Stable Perovskite Solar Cells," *Nature Communications* 15 (2024): 5223.

8. Z. Jiang, F. Ren, Q. Zhou, et al., "Solvent Engineering for Scalable Fabrication of High-Quality Formamidinium Cesium-Based Perovskite Films Toward Highly Efficient and Stable Solar Modules," *Advanced Energy Materials* 15 (2025): 2500598.

9. M. Yang, Z. Li, M. O. Reese, et al., "Perovskite Ink With Wide Processing Window for Scalable High-Efficiency Solar Cells," *Nature Energy* 2 (2017): 17038.

10. H. Gao, K. Xiao, R. Lin, et al., "Homogeneous Crystallization and Buried Interface Passivation for Perovskite Tandem Solar Modules," *Science* 383 (2024): 855.

11. L. Chao, T. Niu, W. Gao, et al., "Solvent Engineering of the Precursor Solution Toward Large-Area Production of Perovskite Solar Cells," *Advanced Materials* 33 (2021): 2005410.

12. Z. Wu, S. Sang, J. Zheng, et al., "Crystallization Kinetics of Hybrid Perovskite Solar Cells," *Angewandte Chemie International Edition* 63 (2024): 202319170.

13. Q. He, P. Liu, H. Li, et al., "Steric Confinement and Dynamic Coordination Synergy for Crystallization Control in 27.9%-Efficient All-Perovskite Tandem Solar Cell," *Advanced Energy Materials* 15 (2025): 2502835.

14. J. Park, S. Kim, Y. H. Chu, et al., "De-Intercalation of Iodoplumbate(DMSO) x Complex for Uniaxially Oriented Halide Perovskite Thin-Film Solar Cells," *Advanced Energy Materials* 14 (2024): 2400620.

15. X. Liao, Y. Zhang, Z. Qu, et al., "Promotion of Grain Growth via Solvent Fumigation for Wide-Bandgap Perovskite Solar Cells With Low VOC Deficit and Perovskite/TOPCon Tandem Solar Cells With Efficiency >30%," *Science Bulletin* 70 (2025): 2997.

16. X. Yang, T. Ma, H. Hu, et al., "Understanding and Manipulating the Crystallization of Sn–Pb Perovskites for Efficient All-Perovskite Tandem Solar Cells," *Nature Photonics* 19 (2025): 426–433.

17. B. Zhao, Z. Du, Y. Xie, et al., "Substitution of DMSO for Stabilized Perovskite Solar Cells With Extended Process Window," *Advanced Functional Materials* 35 (2025): 08262.

18. M. Li, R. Sun, J. Chang, et al., "Orientated Crystallization of FA-Based Perovskite via Hydrogen-Bonded Polymer Network for Efficient and Stable Solar Cells," *Nature Communications* 14 (2023): 573.

19. L. Bi, J. Wang, Z. Zeng, et al., "Temperature-Controlled Vacuum Quenching for Perovskite Solar Modules Towards Scalable Production," *Nature Photonics* 19 (2025): 968–976.

20. M. Ma, C. Zhang, Y. Ma, et al., "Efficient and Stable Perovskite Solar Cells and Modules Enabled by Tailoring Additive Distribution According to the Film Growth Dynamics," *Nano-Micro Letters* 17 (2024): 39.

21. S. Ternes, F. Laufer, and U. W. Paetzold, "Modeling and Fundamental Dynamics of Vacuum, Gas, and Antisolvent Quenching for Scalable Perovskite Processes," *Advanced Science* 11 (2024): 2308901.

22. K. Mo, X. Zhu, M. Yang, et al., "Minimizing DMSO Residues in Perovskite Films for Efficient and Long-Term Stable Solar Cells," *Advanced Energy Materials* 15 (2025): 2404538.

23. S. Chen, X. Dai, S. Xu, H. Jiao, L. Zhao, and J. Huang, "Stabilizing Perovskite-substrate Interfaces for High-performance Perovskite Modules," *Science* 373 (2021): 902–907.

24. M. Wang, C. Fei, M. A. Uddin, and J. Huang, "Influence of Voids on the Thermal and Light Stability of Perovskite Solar Cells," *Science Advances* 8 (2022): abo5977.

25. G. Zhang, B. Ding, Y. Ding, et al., "Suppressing Interfacial Nucleation Competition Through Supersaturation Regulation for Enhanced Perovskite Film Quality and Scalability," *Science Advances* 10 (2024): adl6398.

26. W. Pu, B. Li, Y. Liu, et al., "Cost-Effective Acetonitrile-Based Precursor Solution Mitigates Heterogeneous Nucleation for Efficient and Stable Perovskite Solar Cells," *Small* 20 (2024): 2407706.

27. Y. Liu, B. Ding, Y. Ding, et al., "Fabricating α-$FAPbI_3$ Perovskite Photovoltaics in Ambient Air by DMSO Extraction," *ACS Energy Letters* 9 (2024): 3418–3425.

28. Y. Miao, Y. Chen, H. Chen, X. Wang, and Y. Zhao, "Using Steric Hindrance to Manipulate and Stabilize Metal Halide Perovskites for Optoelectronics," *Chemical Science* 12 (2021): 7231–7247.

29. R. Chen, J. Wang, Z. Liu, et al., "Reduction of Bulk and Surface Defects in Inverted Methylammonium- and Bromide-Free Formamidinium Perovskite Solar Cells," *Nature Energy* 8 (2023): 839–849.

30. S. Fu, N. Sun, H. Chen, et al., "On-Demand Formation of Lewis Bases for Efficient and Stable Perovskite Solar Cells," *Nature Nanotechnology* 20 (2025): 772–778.

31. S. A. Markarian, A. L. Zatikyan, V. V. Grigoryan, and G. S. Grigoryan, "Vapor Pressures of Pure Diethyl Sulfoxide From (298.15 to 318.15) K and Vapor–Liquid Equilibria of Binary Mixtures of Diethyl Sulfoxide With Water," *Journal of Chemical & Engineering Data* 50 (2005): 23–25.

32. O. Romiluyi, Y. Eatmon, R. Ni, B. P. Rand, and P. Clancy, "The Efficacy of Lewis Affinity Scale Metrics to Represent Solvent Interactions With Reagent Salts in All-Inorganic Metal Halide Perovskite Solutions," *Journal of Materials Chemistry A* 9 (2021): 13087–13099.

33. S. Yuan, D. Zheng, T. Zhang, et al., "Scalable Preparation of Perovskite Films With Homogeneous Structure via Immobilizing Strategy for High-Performance Solar Modules," *Nature Communications* 16 (2025): 2052.

34. S. Li, Y. Jiang, J. Xu, et al., "High-Efficiency and Thermally Stable $FACsPbI_3$ Perovskite Photovoltaics," *Nature* 635 (2024): 82–88.

35. W. Wu, H. Gao, L. Jia, et al., "Stable and Uniform Self-Assembled Organic Diradical Molecules for Perovskite Photovoltaics," *Science* 389 (2025): 195.

36. S.-H. Cho, S. C. Cho, S.-J. Chang, S. U. Lee, and N.-G. Park, "Solution-Phase PbI_2 Coordination Controls Perovskite Film Formation and Photovoltaic Performance," *ACS Energy Letters* 10 (2025): 3931–3940.

37. Z. Zhang, J. Liang, J. Wang, et al., "DMSO-Free Solvent Strategy for Stable and Efficient Methylammonium-Free Sn–Pb Alloyed Perovskite Solar Cells," *Advanced Energy Materials* 13 (2023): 2300181.

38. X. Zhang, Y. Luo, X. Wang, et al., "Locking Surface Dimensionality for Endurable Interface in Perovskite Photovoltaics," *Carbon Energy* 7 (2025): 718.

39. H. Zhu, B. Shao, Z. Shen, et al., "In Situ Energetics Modulation Enables High-Efficiency and Stable Inverted Perovskite Solar Cells," *Nature Photonics* 19 (2025): 28–35.

40. R. Nie, P. Zhang, J. Gao, et al., "Enhanced Coordination Interaction With Multi-Site Binding Ligands for Efficient and Stable Perovskite Solar Cells," *Nature Communications* 16 (2025): 6438.

41. M. Chen, Z. Qin, Z. Zhang, et al., "Low-Temperature Sequential Deposition for Efficient Inverted Perovskite Solar Cells," *Nature Communications* 16 (2025): 5746.

42. Y. Zhu, X. Liu, X. Sui, et al., "Intermediate-Phase Homogenization Through Intermolecular Interactions Toward Reproducible Fabrication of Perovskite Solar Cells," *Advanced Energy Materials* 15 (2025): 2500536.

43. W. Li, S. K. Yadavalli, D. Lizarazo-Ferro, et al., "Subgrain Special Boundaries in Halide Perovskite Thin Films Restrict Carrier Diffusion," *ACS Energy Letters* 3 (2018): 2669–2670.

44. Y. Zhou, H. Sternlicht, and N. P. Padture, "Transmission Electron Microscopy of Halide Perovskite Materials and Devices," *Joule* 3 (2019): 641–661.

45. M.-C. Tang, S. Zhang, T. J. Magnanelli, et al., "Unraveling the Compositional Heterogeneity and Carrier Dynamics of Alkali Cation Doped 3D/2D Perovskites With Improved Stability," *Materials Advances* 2 (2021): 1253–1262.

46. J. Suo, B. Yang, E. Mosconi, et al., "Multifunctional Sulfonium-Based Treatment for Perovskite Solar Cells With Less Than 1% Efficiency Loss Over 4500-h Operational Stability Tests," *Nature Energy* 9 (2024): 172–183.

Supporting Information

Additional supporting information can be found online in the Supporting Information section.

Supporting File: adma72483-sup-0001-SuppMat.pdf.

Supporting File: adma72483-sup-0002-VideoS1.